Synthesis of ZnO Nanopartcles by Flame Spray Pyrolysis and Characterisation Protocol

R. Wallace[1], A. P. Brown[1], R. Brydson[1], K. Wegner[2], S. J. Milne[1]

1. Institute for Materials Research, SPEME, University of Leeds, LS2 9JT, UK

2. Particle Technology Laboratory, Department of Mechanical and Process Engineering, ETH Zurich, CH-8092 Zurich, Switzerland

Abstract

This paper reports detailed characterisation of a zinc oxide (ZnO) nanopowder synthesized by a flame spray pyrolysis method. Detailed characterisation of the powder was carried out following a protocol that aims to determine key physicochemical characteristics that may affect its toxicity. Analysis by X-ray diffraction, (XRD), transmission electron microscopy (TEM) and surface area measurements confirmed monophasic hexagonal wurtzite ZnO nanoparticles with a specific surface area of 59 m^2/g. Histograms derived from TEM analysis are presented to illustrate the polydispersity within the sample; particles were elongated in the c-crystallographic direction, with average length ~ 23 nm and width ~14 nm. Dynamic light scattering (0.1 w/v % in deionised water, pH 7.4) revealed the particles were agglomerated with a modal secondary particle size of ~ 1.5 µm. Fourier transform infra-red spectroscopy and X-ray photoelectron spectroscopy indicated the presence of carbonate impurities on the surface of the ZnO nanoparticles.

Introduction

Zinc oxide (ZnO) is a wide band gap semiconductor material (approximately 3.37 eV at 300 K) which has received great interest for its potential applications in the electronics and photonics industries (Johnson et al. 2004; Onreabroy et al., 2006). In addition, ZnO is used in medical and healthcare applications due to its antibacterial behaviour (Zhang et al. 2006). Nano-sized ZnO particles are of particular interest in numerous applications due to performance enhancements associated with nano-dimensions (Padmavathy and Vijayaraghavan, 2008; Yamamoto, 2001). Nanoparticles of ZnO are added to some sunscreens due to the broad range of absorbance both in the UV A and B range (Mitchnick et al. 1999). They exhibit high visible transparency, and superior biocompatibility to organic UV filters (Gustavsson et al. 2002), which has led also to the use of nano ZnO in cosmetics as well as in paints and pigments (Liufu

S. 2005). Synthesis of large quantities of high purity, homogenous nanoparticulate ZnO is therefore important in order to supply the needs of industry.

Nanoparticles of ZnO have been prepared by physical methods, such as milling and grinding, (Shen 2006); by thermal evaporation of ZnO (Wang, 2004) or evaporation and oxidation of zinc (Wu et al., 2000); and by chemical solution synthesis routes such as hydrothermal synthesis (Suchanek, 2009; Baruah and Dutta 2009), sol-gel (Meulenkamp 1998; Mondelaers et al., 2002) and precipitation from both aqueous and non-aqueous solvents (Jézéquel et al., 1995, Hsieh et al., 2007). However, despite the wide variety of wet chemical methods, the majority of ZnO is produced in industry by gas phase synthesis through oxidation of Zn vapour (Auer et al, 2009). Gas phase synthesis is suitable for preparing ZnO nanoparticles with high crystallinity as the reaction occurs at very high temperatures over a short time span.

Flame aerosol synthesis is a promising, scalable alternative gas-phase production method for zinc oxide nanoparticles. Here, a gaseous (vapor-fed aerosol flame synthesis, VAFS), liquid (flame-assisted spray pyrolysis, FASP, and flame spray pyrolysis, FSP) or solid precursor is introduced into a flame and converted to nanoparticles (Teoh et al., 2010). For instance, Jensen et al. (2000) produced ZnO nanoparticles of 25-40 nm diameter via VAFS by subliming zinc acetylacetonate into nitrogen carrier gas and feeding the vapor to a premixed methane-air flame. Matsoukas and Friedlander (1991) introduced an aerosol of solid zinc nitrate particles into a diffusion flame and studied the evolution of the size distribution for the resulting ZnO nanoparticles. However, delivery of a liquid precursor into the flame may be the most effective route, since a broad range of less volatile raw materials is available that can be dissolved in organic solvents or even water, allowing relatively simple liquid precursor handling and dosing. In particular, flame spray pyrolysis (Bickmore et al., 1996; Mädler et al., 2002) that benefits from self-sustaining high temperature flames has been shown to be a versatile and scalable method for the production of single- and multi-component oxide and even metal nanoparticles, as is apparent from recent reviews (Teoh et al., 2010; Athanassiou et al., 2010; Strobel and Pratsinis 2007).

ZnO nanoparticle synthesis with liquid-fed flame reactors in FASP mode has been studied by Marshall et al. (1971), spraying an aqueous solution of zinc acetate into a town gas-air burner. Carroz et al. (1980) produced ZnO nanoparticles of 200 nm diameter by FSP of zinc nitrate solutions in ethanol and methanol. Tani et al. (2002) used FSP to produce zincite nanoparticles employing zinc acrylate as the precursor and methanol as the solvent. Product particle diameters obtained from nitrogen adsorption ranged from 10 nm to 18 nm; size increased as the rate of supply of the precursor solution to the flame increased from 1 ml/min to 4 ml/min. Nanoparticles made at higher precursor flow rates were slightly elongated, in agreement with Strobel and Pratsinis (2011) who observed formation of ZnO nanoparticles with ≈ 1.5 aspect ratio by FSP employing a zinc-nitrate hexahydrate / ethanol solution. Liewhiran and Phanichphant (2007) reported mainly spheroidal ZnO nanoparticles with occasional hexagonal and rod-like structures in FSP synthesis from zinc-naphthenate/toluene/acetonitrile precursors for application in gas sensors. Height et al. (2006) made pure as well as doped ZnO nanoparticles and rods by FSP conversion of a zinc-naphthenate/toluene precursor solution. The undoped ZnO particles were predominantly spherical with individual elongated structures.

There is concern surrounding the potential toxicity of engineered nanomaterials to humans and the environment, a topic which at present is not fully understood. As a consequence, extensive research is currently being conducted aimed at investigating the toxicity of nanomaterials. ZnO nanoparticles produced by FSP have been used for toxicological investigation. George et al. (2010) and Xia et al. (2008) implemented FSP produced nanoparticles into cytotoxicity screening tools and Li et al. (2011) investigated the bacterial toxicity of the particles. The ZnO nanoparticles for the studies were produced by dissolving zinc naphthenate precursor in xylene organic solvent. Although particle size was determined by BET and XRD, there was no statistical analysis of size distribution and morphologies of particles present in the TEM sample. Xia et al. (2008) and George et al. (2010) proposed *in-vitro* toxicological screening to rank engineered nanomaterials for priority *in-vivo* testing and chose FSP-made ZnO nanoparticles as one system to study the induction of cellular responses.

The aim of the present work was to synthesize and thoroughly characterize a set of ZnO nanoparticles that in future could be used for studies aimed at investigating the relationship between particle properties and toxicity. It is essential to develop a protocol to characterize the physicochemical properties of the test powders. Data on toxicity will be reported in future publications. Understanding this relationship was a key aim of the European Union funded project ENNSATOX (www.ennsatox.eu) for which this research was carried out. The ZnO particles for the project were required to be around 20 nm in size with a narrow size distribution. Here we report the synthesis of ZnO nanoparticles by a flame spray pyrolysis technique that has been adapted in order to attempt to produce nanoparticles of this size. The precursor solution comprised zinc naphthenate dissolved in toluene. To properly inform the follow on toxicological investigations, it was essential that a detailed particle characterisation protocol was followed to ensure essential information about the morphology, size, composition and agglomeration state of the particles. The protocol involved the following techniques; X-ray diffraction

(XRD), transmission electron microscopy (TEM), energy dispersive X-ray spectroscopy (EDX), selected area electron diffraction (SAED), Fourier transform infra-red spectroscopy (FTIR), thermal gravimetric analysis (TGA) with evolved gas analysis (EGA), and X-ray photoelectron spectroscopy (XPS) of the dry powder, and dynamic light scattering (DLS) of the powder in suspension.

Experimental

In contrast to the previous studies, zinc naphtenate (STREM; 65% in mineral spirits, 10 wt % Zn) was chosen as the Zn precursor and was diluted with toluene (Sigma Aldrich) to give a Zn concentration of 0.5 mol/l. The precursor solution was delivered to the flame at a rate of 5ml/min with the help of a syringe pump (Lambda, VIT-FIT) and atomized with coflowing 5 l/min of oxygen dispersion gas at 3 bar pressure drop. The oxygen and methane supporting flame feed rates were 2.5 l/min and 1.25 l/min respectively. The flow rates of all gases (PanGas, ≥ 99.5%) were adjusted with calibrated mass flow controllers (Bronkhorst EL-FLOW) and are reported at 25°C and 1 atm. Product nanoparticles were then collected on glass-fiber filters (Whatman GF 6, 254 mm diameter) with the help of a vacuum pump (Busch Seco SV1040).

Phase analysis and crystallite size estimation of the bulk powder was achieved by X-ray powder diffraction (XRD) using a Philips PANalytical X'Pert X-ray diffractometer with a CuKα X-ray source scanning over a range of 5-80° 2θ. Furthermore, the sample was analysed by TEM using a Phillips FEI Tecnai TF20 field emission gun TEM operating at a gun voltage of 200 kV, fitted with an Oxford Instruments INCA 350 energy dispersive X-ray (EDX) system/80mm X-Max silicon drift detector (SDD) and Gatan Orius SC600A charge-coupled device (CCD) camera. Bright field images of the sample were taken to obtain information about particle size and morphology. Energy dispersive X-ray spectroscopy (EDX) was performed on the sample to obtain compositional information and identify any potential impurities. The specific surface area (SSA) of product powders was measured using N_2 gas adsorption employing the BET isotherm. The BET-equivalent diameter of the particles was calculated assuming monodisperse spheres and a zinc oxide density of 5.606 g/cm^3 from eq. 2:

$$d_{BET} = 6000 / (SSA \times \rho), \qquad \text{(Eq. 2)}$$

where d_{BET} is the average primary particle size (nm), SSA the specific surface area (m^2/g) and ρ the density of ZnO (g/cm^3).

A Thermo Scientific IS10 Fourier transform infrared spectrometer (FTIR) with an attenuated total reflection accessory (ATR) was employed to identify carbonate, hydroxyl or other contaminants. A Shimadzu TGA 50 thermogravimetric analyser was used to monitor any changes in mass when the ZnO powder was heated, to further investigate phase purity. Evolved gases were analysed by a Thermo Scientific IS10 FTIR spectrometer with a Thermo Scientific FTIR/TGA interface attached. The sample was heated from 10˚C to 800°C, at a rate of 10°C/min in air; an FTIR spectrum was acquired every minute in order to identify the gases evolved. X-ray photoelectron spectroscopy (XPS) was carried out to investigate the presence of impurities on the surface of the sample, complimenting FTIR studies. XPS measurements were performed using a VG Escalab 250 XPS with monochromated aluminium K-α X-ray source (Spot size diameter = 500 µm; Power = 150 W). The binding energy scale was calibrated by setting the carbon 1s peak to 285 eV. Spectra were analysed using mixed Gaussian-Lorentzian peak fitting within the processing software CasaXPS. Dynamic light scattering (DLS) measurements were carried out using a Malvern Zetasizer Nano ZS instrument and data manipulation was performed by the DTS Nano software to determine the particle size distribution. The powder was dispersed in deionised MilliQ water (with a resistivity of 15 MΩ.cm) at a concentration of 0.1 % w/v. The suspension was then ultrasonically agitated for 20 minutes, before DLS analysis.

Results and Discussion

The XRD pattern collected from the synthesised powder is shown in Figure 1 with the Miller indices of the planes indicated above each peak. The pattern is consistent with that from the JCPDS reference file for the hexagonal-close-packed Wurtzite structure of zincite (ref: 01-079-0206), see Table 1, that has also been observed in other flame-synthesized ZnO powders (Tani et al., 2002; Height et al., 2006; Liewhiran et al., 2007). The average crystallite size was estimated from each of the peaks using the Scherrer equation (Cullity, 2001) and using all of the values obtained, an average crystallite size of 22 nm was calculated. The (0002) peak was slightly narrower than the other peaks indicating a slightly larger crystallite size along these planes. This may be attributed to the presence of a number of elongated particles in the sample, as ZnO grows favourably in the [0001] direction, as is confirmed by TEM below. The specific surface area was determined as 59.0 m^2/g corresponding to an average primary particle diameter of 18 nm which is in good agreement with XRD crystallite size estimation and indicates that particles are predominantly single crystals.

The crystallite and primary particle sizes here are consistent with Height et al. (2006) using the same precursor solution and reactant flow rates but an additional 5 l/min of oxygen sheath gas. For undoped ZnO nanopowder they obtained a specific surface area of 53 m^2/g while the average crystallite sizes determined from the (0002) and (1010) peaks were 27 and 18 nm, respectively. The additional oxygen sheath gas in the experiments of Height et al. (2006) might have resulted in a hotter flame and slightly larger particles by increased particle residence times in the flame. Liewhiran and Phanichphant (2007) obtained somewhat smaller average primary particle and crystallite sizes of 16.8 nm (63.8 m^2/g) and 18 nm, respectively, but used a toluene /acetonitrile (ΔH_C=-1256 kJ/mol) solvent mixture with lower enthalpy of combustion compared to pure toluene (ΔH_C=-3910 kJ/mol) at otherwise similar synthesis conditions. Thus, smaller particles grown in shorter and colder flames are expected. Interestingly, Tani et al. (2004) produced similar-sized particles with 58 m^2/g from a methanol-based solution fed at 4 ml/min and dispersed with 3.85 l/min oxygen (pilot flame: 1.58 l/min CH_4 and 1.52 l/min O_2). Given the low combustion enthalpy of methanol (ΔH_C= -726.1 kJ/mol) and shorter high temperature residence times, smaller product primary particles than from the toluene-based flame here would have been expected.

TEM images of the ZnO nanoparticles show the interparticle variation in size and morphology to have only a small distribution (Figure 2). The inset in Fig. 2(a) is of the selected area electron diffraction of the cluster of particles visible in Figure 2(a). The d-spacings in the material, calculated from measurement of the ring diameters in the SAED pattern shown in Figure 2(a), are in good agreement with XRD data for Zincite (ref: 01-079-0206). The high resolution TEM image in Figure 2(b) shows the clearly discernible lattice planes of a highly crystalline material. The indicated d-spacing of these planes is 2.819 Å which corresponds to the d-spacing of the $\{10\overline{1}0\}$ planes of the ZnO crystal (JCP-DS ref: 01-079-0206). This indicates that the preferred direction of growth of the elongated ZnO particles is in a direction parallel to the $\{10\overline{1}0\}$ planes, supporting the assumption that the ZnO nanoparticles in this sample grow preferentially along the c-axis, <0001>, as is typically observed with gas-phase synthesis techniques (Wang, 2004). The widths and lengths of 250 particles were measured and the data are presented in histograms (Figure 3). Figure 3 (a) shows the distribution of particle lengths with an average value of 23 nm and a median of 22 nm. Figure 3 (b) shows the distribution of particle widths with an average value of 14 nm and a median of 12 nm. The Feret ratios for each particle measured are presented in Figure 3 (c) and the data indicate that the majority of particles are elongated with an average Feret ratio of 1.6. The Feret ratio histogram is skewed positively with a median value of 1.4 and mode of 1.3, indicating that the majority of the particles have a lower Feret ratio than the mean suggests, consistent with the TEM image shown in Figure 2(a). Taking into account the average particle lengths and widths, the size values are in good agreement with both BET and XRD crystallite size determinations. The particle morphologies here qualitatively resemble those observed by Liewhiran and Phanichphant (2007) even though the authors reported mainly spheroidal with occasional hexagonal and rod-like particles consistent with Height et al. (2006). The ZnO nanoparticles obtained by Tani et al. (2000) at their highest precursor feed rate of 4 ml/min are also elongated, but no aspect ratio was reported. Strobel and Pratsinis (2011) qualitatively estimated an aspect ratio of 1.5 for their ZnO particles from zinc nitrate precursor solutions. These results show that average primary particle or crystallite size data is insufficient to characterize flame-made zinc oxide nanopowders but a quantitative particle size and shape analysis should be carried out.

Particle size distribution data obtained by DLS for nanoparticles suspended in water at a final solution pH of 7.4, are shown in Figure 4. The light scattering profile of the suspension is converted into plots of intensity, volume and number using the instrumental software. The Rayleigh approximation states that the intensity of light scattered by a particle is proportional to the diameter of the particle ($I \alpha d^6$). The intensity profile in Fig. 4(a) displays a modal peak at 1500 nm, a secondary peak at 185 nm and two smaller peaks at 550 and 5500 nm. The intensity plot shows the relative intensity of light scattered by each of the size groups. The volume profile displayed in Figure 4 (b) has a modal peak at 180 nm, a secondary peak at 1500 nm and two smaller peaks at 550 nm and 5500 nm. The volume plot is formed by conversion of the intensity profile using Mie theory which takes into account the greater relative scattering of the larger particles compared to the small (Malvern, 2000), and hence explains the switch between the relative size of modal and secondary peaks. The number profile shown in Fig. 4(c) is derived from the volume plot and displays the relative percentage of particles in each size class. The number plot displays the narrowest particle size distribution, however as it is derived using a mathematical approximation and is not necessarily the most accurate. The plot has a principal peak at 160 nm indicating that the majority of the nanoparticles (with an average primary particle size of 18 nm) in the suspension are agglomerated into clusters of particles. The secondary peak at 500 nm accounts for a much smaller fraction of larger agglomerates present in the suspension. Although the number profile indicates that the majority of the agglomerates present in the sample are below 800 nm, it does not show the extremely low fraction of agglomerates present that are greater than 1000 nm in hydrodynamic diameter, as shown by the intensity and volume plots.

The DLS measurements were taken immediately after the sample was removed from the ultrasonic bath and are therefore not an indication of how well the particles are dispersed with time. The suspension is unstable with the particles sedimenting within minutes of being removed from the ultrasonic bath. This can be explained by the solution pH of 7.4 which is relatively close to the isoelectric point of ZnO at pH 8.4. ADD REF Particle stability must be taken into account in toxicological assays which invariably take place in a liquid medium. The degree of particle agglomeration in suspensions will be affected by the dispersing medium i.e. the presence of salts and protein serum can affect nanoparticle stability (Hondow et al. 2012).

Figure 5(a) shows the FTIR spectrum obtained for the as-prepared sample. The strong band ≤ 550 cm^{-1} is characteristic of the broad band of absorption that indicates ZnO lattice bonding (Umar et al., 2009; Wahab et al.; 2009, Li et al., 2010). The band at ~ 1700 cm^{-1} is characteristic of C=O stretching of an organic carbonyl group. It may be due to aldehyde, ketone or carboxylic acid compounds that have formed due to partial decomposition of the precursor compound zinc napthtenate in the toluene-fuelled flame during the synthesis process. The band at 3400 cm^{-1} relates to the O-H stretch of the hydroxyl vibration and hence indicates hydration of the sample. Literature reports that the characteristic band here for O-H occurs between 3200-3600 cm^{-1} (Socrates, 2001), however the band present in the current sample spectrum continues down to 2800 cm^{-1}. It is likely that the O-H band is masking another absorption band that can most probably be attributed to the asymmetrical stretch of a C-H bond present in the carbonyl containing compound mentioned above. The overlapping bands at 1400, 1250 and 750 cm^{-1} are characteristic of inorganic carbonate which are known to have absorption bands at 1160 cm^{-1}, 1100-1040 cm^{-1} and between 900-800 cm^{-1} (Socrates, 2001; Chowdury et al.). This is likely to be present as a result of absorbed CO_2.

The FTIR spectrum in Fig 5(b) is of an aged sample of the powder and, as expected, the bands occurring as a result of sample hydration and carbonation increase in strength. Formation of surface carbonates and hydroxides is typically observed with zinc oxide exposed to ambient air since $ZnCO_3$ is a stable phase if CO_2 is present, while $Zn(OH)_2$ is close to stability in humid air (Klimm et al., 2011). Thus it must be taken into account that ZnO surfaces exposed to air may easily form layers of carbonate and/or hydroxide not only by adsorption but also by chemical reaction (Klimm et al., 2011). The FTIR spectrum in Fig. 5(c) was obtained immediately after the sample had been heated to 950°C in order to investigate whether the presence of carbonate, hydroxyl and potential organic contaminants on the surface were diminished. The O-H, C=O and C=H peaks were no longer detectable, suggesting that all of the moisture, as well as the substance responsible for the suspected C=O and C-H bands, was removed during high temperature heat treatment. However, heating the sample to this temperature causes the nanoparticles to sinter into larger particles (Figure 8). A sharpening and decrease in intensity of absorbances due to inorganic carbonate bands is observed indicating a reduction, but not removal of the surface carbonate phase. Either the treatment temperature was still too low for full chemical decomposition of the carbonate, since a ZnO wafer showed a well-structured surface only after annealing at 1150°C in oxygen (Klimm et al., 2011), or the entire surface-carbonate was removed during heat treatment but transferral from the furnace to the FTIR instrument resulted in a limited degree of re-carbonation even in the short time the surface was exposed to air.

XPS was carried out in order to investigate the surface composition of the ZnO nanoparticles in greater detail. XPS is usually carried out on a graphite substrate, however as the carbon content in the sample was of interest, indium was used instead. XPS was performed close to the time of synthesis of the sample (T=1 month), and then again 8 months later (T=9 months) in order to investigate the extent to which the sample was absorbing atmospheric CO_2. The C_{1s} region of the XPS spectra for both samples are shown in Figure 6 and indicate that the carbon content increases substantially, in agreement with FTIR analyses on ageing. Three different carbon species are identified by XPS, each of which can be identified by the binding energy at which the peak occurs. The peak at 285 eV corresponds to a C-H bonded C atom and the peak at 288.9 eV is indicative of a carbon in a carboxylic acid, ketone or aldehyde (already suggested by FTIR). The peak at 286.5 eV is likely to be indicative of absorbed CO_2 to form $ZnCO_3$ on the nanoparticle surface. This is also consistent with the FTIR findings (Fig. 5). The estimated amount of carbonate species present in the analysed surface region of the sample, expressed as a percentage of total carbon content, increases from 10 % at T = 1 month to 25 % at T = 8 months. This carbonate/hydroxide layer can constitute a significant weight fraction of high surface area nanoparticles and significantly affect their chemical and physical properties. Solubility for example is emerging as a key factor in understanding ZnO toxicity (Reed et al., 2012; Xia et al., 2008).

Figure 7(a) shows the results of a TGA experiment performed on the sample with the mass expressed as a percentage of the total initial starting mass. Evolved gas analysis was performed on the sample in order to confirm the composition of the gases evaporating from the sample during TGA. The Gram-Schmidt plot shown in Figure 6(b) shows how the total IR absorbance changes as the temperature rises. The reduction in mass observed in Figure 7(a) can be explained by the increase in overall absorbance observed in the Gram-Schmidt plot (Figure 7(b)). The steep drop observed in Fig. 7(a) between 50°C and 150°C in which the sample loses around 1.5% of its total mass can be explained by water vapour, already identified by FTIR, evaporating from the sample. Evidence for this is observed in Figure 7(c) which shows the absorbance detected in the range 1500-1900 cm^{-1}, indicative of O-H bending, increasing in intensity over the same temperature range, 50°C to 150°C. There is then a more gradual reduction in weight between 150 and 650°C where the sample loses around 2% of its total mass. This may be surface zinc carbonate, which has already been identified by FTIR and XPS, decomposing to form carbon dioxide. Evidence for this is observed in Figure 7(d) which shows two peaks of absorbance in the range 2250-2400 cm^{-1}, indicative of carbon dioxide evolving between 200 and 500°C. There is a possibility that CO_2 may also be formed by decomposition of residual organic precursors present on the surface of the particles, for which there was evidence from XPS and FTIR. During synthesis, the maximum flame temperature is around 2200 - 2700°C (Mädler et al., 2002; Gröhn et al., 2012), yet out investigations infer that some of the precursor derivatives do not fully decompose. This may be because the particles experience the flame temperature for a fraction of a second, whereas in TGA analysis, despite the lower temperatures the dwell times are much longer (heating rate 10°C/s) enabling decomposition reactions to proceed to completion. Moreover, Gröhn et al. (2011) also observed individual precursor droplets escaping the spray that might contaminate the product ZnO nanoparticles on the collection filter.

Figure 8(a) shows a TEM image of the sample after heating to 800°C for TGA and reveals that the particles have sintered into larger entities with an average particle size of around 250 nm. The crystalline structure of the powder does not change however, as the ring pattern in Figure 8(b) confirms hexagonal phase zincite.

In summary, the characterisation protocol followed in this study has provided detailed information on the particle size and morphology, structure, and surface composition of the FSP ZnO nanoparticles. This information is essential to better understand the relationship between nanoparticle properties and any toxic effects they may exhibit. This protocol involved X-ray diffraction (XRD), BET specific surface area analysis, transmission electron microscopy (TEM), energy dispersive X-ray spectroscopy (EDX), selected area electron diffraction (SAED), Fourier transform infra-red spectroscopy (FTIR), thermal gravimetric analysis (TGA) with evolved gas analysis (EGA) and X-ray photoelectron spectroscopy (XPS) of the dry powder and dynamic light scattering (DLS) of the powder suspended in MilliQ water. The results obtained for each of the techniques, are summarised in Table 2. The protocol may be used in future studies for the purposes of characterising nanoparticle samples for toxicological studies.

For the ZnO powder, XRD and BET techniques gave average particle sizes in good agreement, ~ 18-22 nm nm. However, the value determined from these techniques uses formulae that assume spherical particles. The narrower FWHM for the 0002 peak of the XRD plot indicated that there were elongated particles present in the sample that grew preferentially along the <0001> axis. Quantitative particle analysis by TEM imaging revealed elongated nanoparticles with an average Feret ratio of 1.6. These results highlight the importance of characterising a sample using TEM to determine a detailed overview of the distribution of sizes and morphologies present in a sample. Suspensions were thoroughly mixed prior to drop casting TEM grids, to increase the probability that TEM samples were representative. Individual measurements of 250 particles enabled histograms to be produced which indicated the polydispersity in size and shape within the TEM specimen. This additional information on particle size and shape will be invaluable when comparing toxicology results for different powders. Solubility studies in relevant biological media would complement the detailed basic physio-chemical characterisation reported here (Xia, 2008).

FTIR, XPS and TGA revealed the presence of various forms of carbon species present in the material. It is likely that these compounds are a result of carbonation of the surface of the nanoparticles from storage in air, and although inconclusive at present, there may be organic compounds present formed by combustion of the precursors used in the synthesis procedure. Another possible source of contamination of the sample may have arisen from the glass-fiber filters on which the particles are collected during synthesis, which contain an organic binder. The use of toluene as the precursor solvent combined with a faster feed rate of 5 ml/min did not appear to produce particles significantly larger than those synthesized by Tani et al. (2009).

Conclusions

ZnO nanoparticles have been synthesised for by a flame spray pyrolysis technique, and a characterisation protocol implemented to determine the physicochemical properties of the powders. Many of the hexagonal wurtzite ZnO particles were elongated in the c -direction: mean particle lengths were 23 nm and widths 14 nm. Surface areas were 59 m^2/g. Carbonate and hydroxide surface phases were identified using a combination of Fourier transform infra red spectroscopy, thermogravimetric analysis and X-ray photoelectron spectroscopy. Impurities such as these may alter the physical and chemical behaviour of the nanoparticles, and must be taken into account in future toxicity studies.

References

Athanassiou E K, Grass R N, Stark W J (2010) Chemical aerosol engineering as a novel tool for material science: From oxides to salt and metal nanoparticles. Aerosol Sci Technol 44:161-172.

Auer G, Woditsch P, Westerhaus A, Kischkewitz J, Griebler W-D, De Liedekerke M (2009) Pigments, Inorganic, 2. White Pigments. In: Ullmann's encyclopedia of industrial chemistry, 6th edn. Wiley, Weinheim, Vol. 27, pp 286-289.

Baruah S, Dutta J (2009). Hydrothermal growth of ZnO nanostructures. Sci. Technol. Adv. Mater. 10: 013001.

Bickmore CR, Waldner KF, Treadwell DR, Laine RM (1996) Ultrafine spinel powders by flame spray pyrolysis of a magnesium aluminum double alkoxide. J Am Ceram Soc 79: 1419-1423.

Carroz J W, Odencrantz F K, Finnegan W G, Drehmel DC (1980) Aerosol generation to simulate specific industrial fine particle effluents. Am Ind Hyg Assoc J 41:77-84.

George S, Pokhrel S, Xia T, Gilbert B, Ji Z, Schowalter M, Rosenauer A, Damoiseaux R, Bradley KA, Mädler L, Nel AE (2010) Use of a rapid cytotoxicity screening approach to engineer a safer zinc oxide nanoparticle through iron doping. ACS Nano 4:15-29.

Gröhn AJ, Pratsinis SE, Wegner K (2012) Fluid-particle dynamics during combustion spray aerosol synthesis of ZrO_2. Chem Eng J 191:491-502.

Gustavsson, Gonzalez H., Farbrot, A., Larko, O. (2002) Percutaneous absorbtion of benzophenone-3, a common component of topical sunscreens. Clinical and Experimental Dermatology 27, 691.

Height MJ, Mädler L, Pratsinis SE, Krumeich F (2006) Nanorods of ZnO made by flame spray pyrolysis. Chem Mater 18: 572-578.

Jensen JR, Johannessen T, Wedel S, Livbjerg H (2000) Preparation of ZnO – Al2O3 particles in a premixed flame. J Nanoparticle Res 2:363-373.

Jézéquel D, Guenot J, Jouini N, Fiévet F (1995) Submicrometer zinc oxide particles: Elaboration in polyol medium and morphological characteristics. J Mater Res 10:77-83.

Johnson J. C., Knutsen K. P., Yan H., Law M., Zhang Y, Yang P, and Saykally R J, (2004) Ultrafast Carrier Dynamics in Single ZnO Nanowire and Nanoribbon Lasers, *Nano Letters* 4 (2) 197-204.

Klimm D, Schulz D, Ganschow S (2011) Growth of bulk ZnO, *Comp. Semicond. Sci. Tech.* (3) 302-338.

Li, Y., K. Wu, and I. Zhitomirsky. 2010. "Electrodeposition of composite zinc oxide–chitosan films." *Colloid. Surface. A:* 356(1-3):63-70.

Li M, Pokhrel S, Jin X, Mädler L, Damoiseaux R, Hoek EMV (2011) Stability, bioavailability, and bacterial toxicity of ZnO and iron-doped ZnO nanoparticles in aquatic media. Environ Sci Technol 45:755-761.

Liewhiran C, Phanichphant S (2007) Influence of thickness on ethanol sensing characteristics of doctor-bladed thick film from flame-made ZnO nanoparticles. Sensors 7: 185-201.

Liufu, S., Xiao, H., & Li, Y. (2005). Effect of MA-Na copolymer adsorption on the colloidal stability of nano-sized ZnO suspension. *Materials Letters*, *59*(27), 3494-3497.

Mädler L, Kammler HK, Mueller R, Pratsinis SE 2002. Controlled synthesis of nanostructured particles by flame spray pyrolysis. J Aerosol Sci 33:369-389.

Malvern. 2000. *Dynamic Light Scattering: An Introduction in 30 Minutes*.

Marshall BS, Telford I, Wood R (1971) A field method for the determination of zinc oxide fume in air. Analyst 96:569-578.

Matsoukas T, Friedlander SK (1991) Dynamics of aerosol agglomerte formation. J Colloid Interface Sci 146: 495-505.

McCarthy JF, Yurek GJ, Elliot JF, Amdur MO (1982) Generation and characterization of submicron aerosols of zinc oxide. Am Ind Hyg Assoc J 43:880-886.

Meulenkamp EA (1998) Synthesis and growth of ZnO nanoparticles. J Phys Chem B 102:5566-5572.

Mitchnick, M., Fairhurst, D., & Pinell, S. (1999). Microfine zinc oxide (Z-Cote) as a photostable UVA/UVB sunblock agent. *Journal of the American Academy of Dermatology*, *40*(1), 85-90.

Mondelaers D, Vanhoyland G, Van den Rul H, D'Haen J, Van Bael MK, Mullens J, Van Pouke LC (2002) Synthesis of ZnO nanopowder via an aqueous acetate-citrate gelation method. Mater Res Bull 37:901–914.

Padmavathy, N., & Vijayaraghavan, R. (2008). Enhanced bioactivity of ZnO nanoparticles—an antimicrobial study. *Science and Technology of Advanced Materials*, *9*(3), 035004.

Shen l, Bao N, Yanaglsawa K, Domen K, Gupta A, Grimes C A (2006) Direct synthesis of ZnO nanoparticles by a solution-free mechanochemical reaction. *Nanotechnology* 17(20):5117-5123.

Strobel R, Pratsinis SE (2007) Flame aerosol synthesis of smart nanostructured materials. J Mater Chem 17:4743-4756.

Strobel R, Pratsinis SE (2011) Effect of solvent composition on oxide morphology during flame spray pyrolysis of metal nitrates. Phys Chem Chem Phys 13: 9246-9252.

Sturgis CC, Drinker P, Thomson RM (1927) Metal fume fever. I. Clinical observations on the effect of the experimental inhalation of zinc oxide by two apparently normal persons. J Indust Hygiene 9:88-97.

Suchanek WL (2009) Systematic study of hydrothermal synthesis of zinc oxide (ZnO) nano-sized powders with superior UV attenuation. J Crystal Growth 312: 100-108.

Tani T, Mädler L, Pratsinis SE (2002) Homogeneous ZnO nanoparticles by flame spray pyrolysis. J Nanoparticle. Res. 4: 337-343.

Teague SV, Raabe OG (1980) Generation of fume aerosols of zinc oxide. *Am. Ind. Hyg. Assoc. J.* 41: 680-683.

Teoh WY, Amal R, Mädler L (2010) Flame spray pyrolysis: An enabling technology for nanoparticles design and fabrication. *Nanoscale.* 2: 1324-1347.

Ahmad U, Rahman MM, Vaseem M, and Hahn YB. 2009. "Ultra-sensitive cholesterol biosensor based on low-temperature grown ZnO nanoparticles." *Electrochem. Commun.* 11(1):118-121.

Wahab, Rizwan, S.G. Ansari, Young Soon Kim, Minwu Song, and Hyung-Shik Shin. 2009. "The role of pH variation on the growth of zinc oxide nanostructures." *Applied Surface Science* 255(9):4891-4896.

Wang, Z. L. (2004). Zinc oxide nanostructures: growth, properties and applications. *Journal of Physics: Condensed Matter*, *16*(25), R829-R858.

Wu R, Xie C, Xia H, Hu J, Wang A (2000). The thermal physical formation of ZnO nanoparticles and their morphology. J Crystal Growth 217:274-280.

Xia T, Kovochich M, Liong M, Mädler L, Gilbert B, Shi H, Yeh JI, Zink JI, Nel AE (2008) Comparison of the mechanism of toxicity of zinc oxide and cerium oxide nanoparticles based on dissolution and oxidative stress properties. ACS Nano 2:2121-2134.

Yamamoto, O. (2001). Influence of particle size on the antibacterial activity of zinc oxide. *International Journal of Inorganic Materials*, *3*(7), 643-646.

Synthesis by Flame Spray Pyrolysis and Characterisation Protocol for ZnO nanoparticles

R. Wallace[1], A. P. Brown[1], R. Brydson[1], K. Wegner[2], S. J. Milne[1]

1. Institute for Materials Research, SPEME, University of Leeds, LS2 9JT, UK

2. Particle Technology Laboratory, Department of Mechanical and Process Engineering, ETH Zurich, CH-8092 Zurich, Switzerland

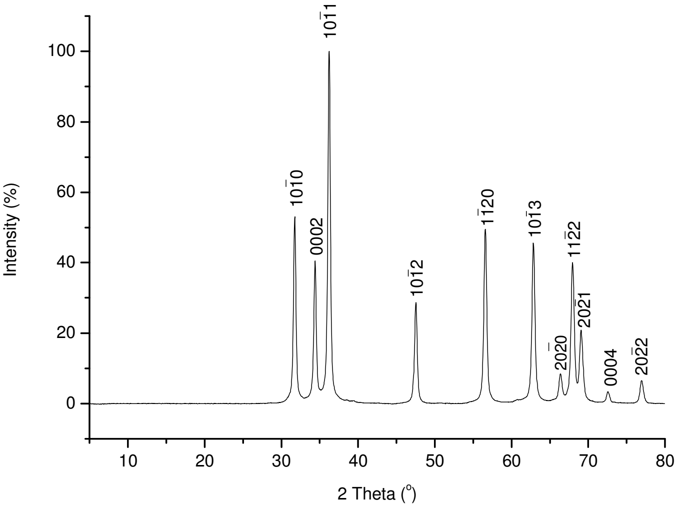

Figure 1: XRD pattern for ZnO nanopowder with the Miller indices for the reflecting plane labelled.

Table 1: XRD peak positions for the synthesized ZnO powder (Fig. 1). Also listed are the referenced values for zincite extracted from the JCPDS file, 01-079-0206.

Number	***hkil***	**2θ(°)**		**d-spacing (Å)**		**Relative Intensity (%)**	
		JCPDS Reference 01-079-0206	**Experimental XRD Pattern**	**JCPDS Reference 01-079-0206**	**Experimental XRD Pattern**	**JCPDS Reference 01-079-0206**	**Experimental XRD Pattern**
1	$10\bar{1}0$	31.77	31.72	2.815	2.819	57.6	53.1
2	0002	34.42	34.42	2.603	2.604	41.4	40.1
3	$10\bar{1}1$	36.25	36.23	2.476	2.477	100	100
4	$10\bar{1}2$	47.54	47.53	1.911	1.911	21.4	28.7
5	$11\bar{2}0$	56.60	56.59	1.625	1.625	30.7	50.0
6	$10\bar{1}3$	62.86	62.83	1.477	1.478	26.4	45.7
7	$20\bar{2}0$	66.37	66.36	1.407	1.407	4.00	8.6
8	$11\bar{2}2$	67.95	67.95	1.378	1.378	21.7	40.0
9	$20\bar{2}1$	69.09	69.06	1.359	1.359	10.5	21.0
10	0004	72.57	72.57	1.302	1.302	1.6	3.51
11	$20\bar{2}2$	76.96	76.95	1.238	1.238	3.3	6.62

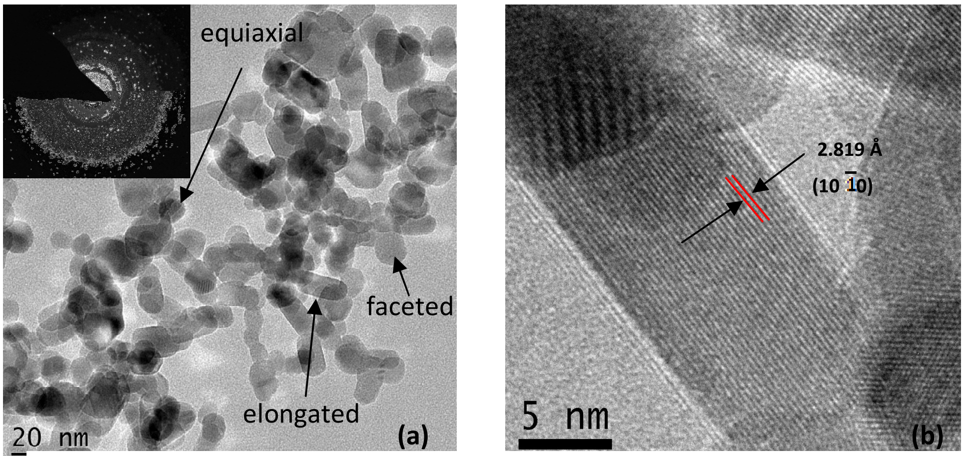

Figure 2: TEM images of: (a) a typical cluster of particles showing varying morphologies present in the sample and with the SAED pattern for the same region of particles inset; (b) an atomic lattice image of an elongated ZnO nanoparticle, with the 10ˉ10 lattice

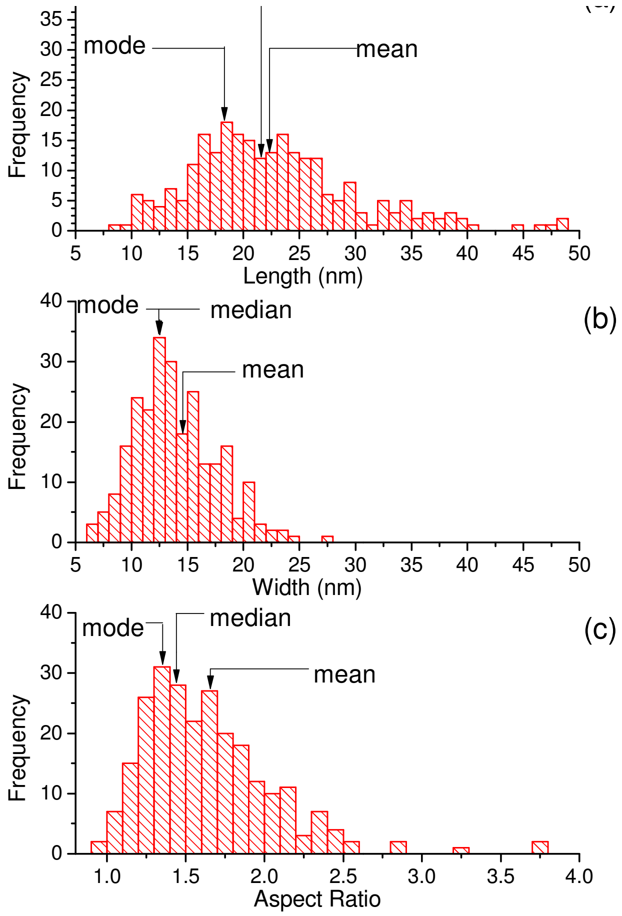

Figure 3: Histograms to show the variation in particle (a) Feret ratio, (b) width and (c) length.

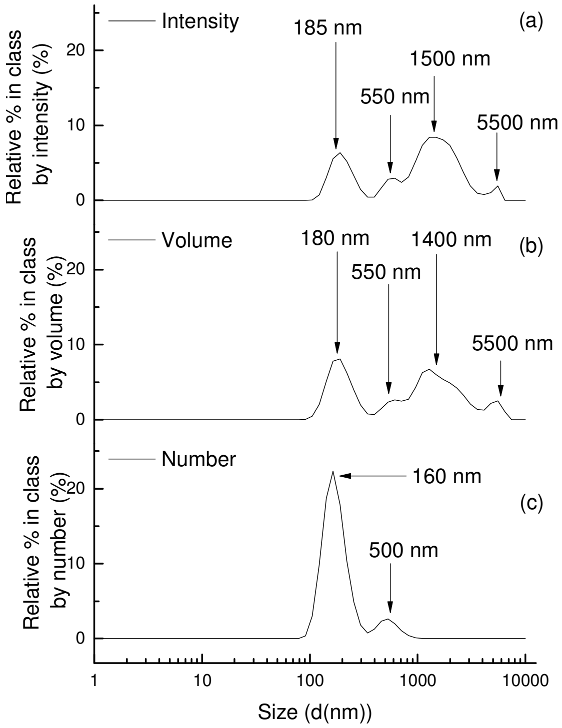

Figure 4: Light scattering profile for a 0.1 % w/v suspension of ZnO nanoparticles dispersed in MilliQ water by (a) intensity, (b) volume and (c) number.

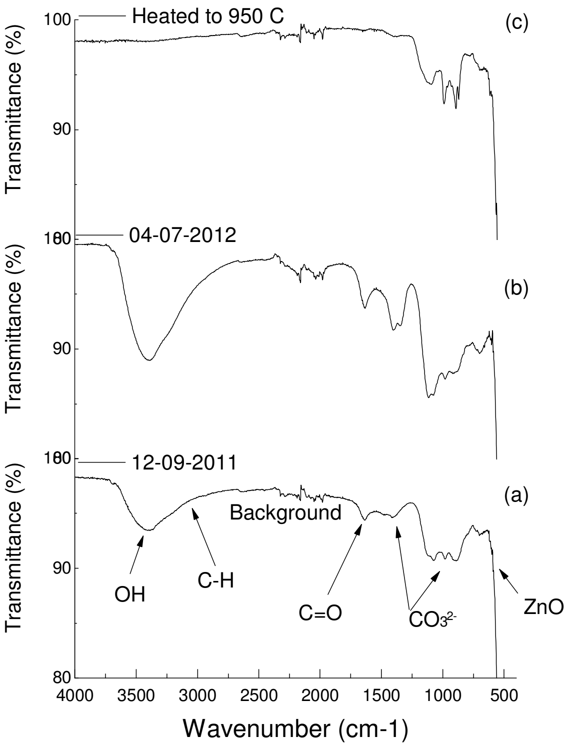

Figure 5: FTIR spectrum for the ZnO nanopowder (a) shortly after preparation, (b) after ageing showing the increase in adsorbed water molecules and carbon dioxide on the surface and (c) after heating to 900°C showing evidence for the elimination of the O-H band and the organic carbonyl peaks previously observed.

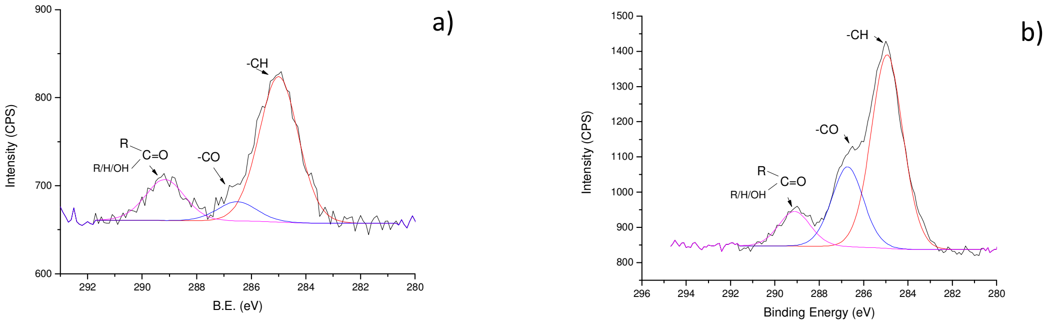

Figure 6: C1s region of the XPS spectra for both FSP 18 at (a) T = 1 month and (b) T = 9 months. Percentages of carbonate species present expressed as a percentage of total carbon, derived from the peak fitting are 10% at T=0 and 25% at T = 9 months.

Table 2: Summary of characterisation protocol and the information obtained from each technique.

Characterisation technique	Information Obtained					
	Average Particle Size	Morphology	Phase	Compsition and Purity	Agglomeration State	Comments
XRD	22 nm	Elongated particles present	Zincite	–	–	Bulk sample analysis; particles grow preferentially in the <0001> direction
BET	18 nm	–	–	–	–	S.S.A. = 59 m^2/g; Bulk sample analysis
TEM	Length = 23 nm; Width = 14 nm	Elongated, equiaxial, spherical.			Particles appear agglomerated in images.	Preferntial growth of particles along c-axis; very small sample size being analysed.
EDX				Zn and O in spectra; No unaccounteable elements present.	–	
SAED			Zincite		–	
FTIR			–	$ZnCO_3$, $ZnOH_2$, H_2O, possible contamination from precursor	–	Probes only the surface of the sample

Characterisation technique	Information Obtained					
	Average Particle Size	Morphology	Phase	Compsition and Purity	Agglomeration State	Comments
TGA			–	Sample loses mass as a result of decomposition of surface contaminants and loss of moisture.	–	Particles are sintered after heat treatment to 800^{o}C
EGA				Sample evolves H2O and CO_2 when heated as a result of contamination.	–	
XPS				$ZnCO_3$, $ZnOH_2$, H_2O, possible contamination from precursor	–	Probes only the surface of the sample
DLS					Agglomertes present in suspension with an average size of 160 nm. Sizes of agglomerates range from a few particles clustered together to over 1000 nm in diametre.	DLS performed immediately after sonication.

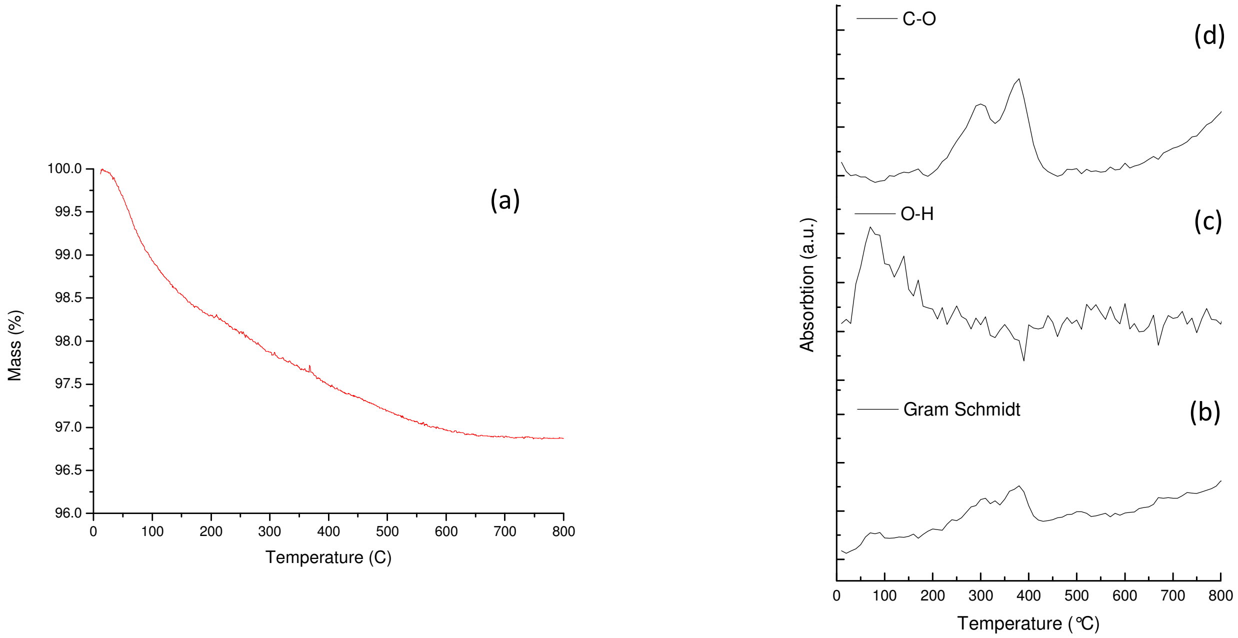

Figure 7: (a) Plot from TGA showing the mass of the sample decreasing continuously as the temperature is increased up to 800°C, at a rate of 10°C /min. (b) Gram-shmidt total absorbance (c) O-H absorbance and (d) C-O absorbance plotted against temperature.

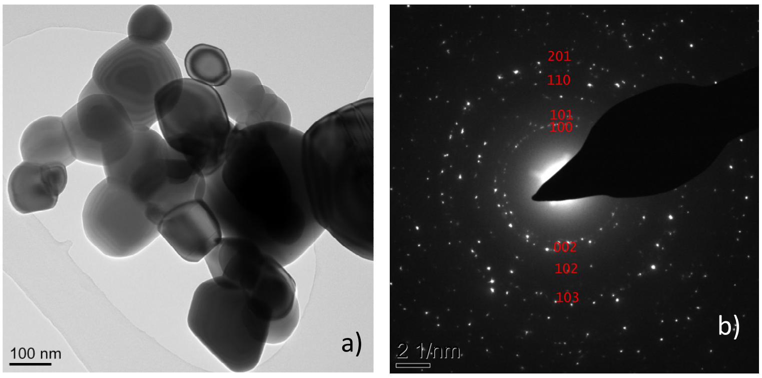

Figure 8: (a)TEM image and (b) SAED pattern showing the sintered ZnO nanoparticles after they have been heated to 800°C for TGA.